Crystal and magnetic structure of orthorhombic $HoMnO_3$

H. W. Brinks,[1] J. Rodríguez-Carvajal,[2] H. Fjellvåg,[1] A. Kjekshus,[1,*] and B. C. Hauback[3]
[1]*Department of Chemistry, University of Oslo, P.O. Box 1033 Blindern, N-0315 Oslo, Norway*
[2]*Laboratoire Léon Brillouin (CEA-CNRS), CEA/Saclay, 91191 Gif sur Yvette Cedex, France*
[3]*Institute for Energy Technology, N-2007 Kjeller, Norway*
(Received 18 August 2000; published 7 February 2001)

o-$HoMnO_3$ crystallizes in the $GdFeO_3$-type structure (*Pbnm*) with no crystal structure anomalies below 295 K and with the Mn-O-Mn angle as low as 144.1°. The Mn^{3+} and Ho^{3+} magnetic moments are ordered below $T_N = 38$ K and $T_{Ho} = 11$ K, respectively. The ordering is incommensurate with a propagation vector $\mathbf{k} = k_y\mathbf{b}^*$, where k_y is between 0.395 and 0.431 depending on temperature. Symmetry analyses have been carried out for both magnetic sites. The ordering was determined to be A_y for the Mn^{3+} moments, modulated in a longitudinal sinusoidal wave along the propagation vector. The Ho^{3+} moments order with the same propagation vector as Mn^{3+}, but the site is split in two orbits of two ions, each ordered in an $a_x f_y$ pattern with a phase factor between them. At the lowest temperatures an antiferromagnetic (commensurate) magnetic phase appears in competition with the main (incommensurate) magnetic phase. The arrangement of the moments is discussed in terms of the magnetic exchange interactions and compared with the closely related magnetic structures of $LaMnO_3$, $TbMnO_3$, and *o*-$YMnO_3$. k_y is found to increase with decreasing size of the rare-earth component.

DOI: 10.1103/PhysRevB.63.094411 PACS number(s): 75.30.Et

I. INTRODUCTION

Perovskite phases with the formula $R_{1-x}A_xBO_3$ (R = La, Pr, Nd; A = Ca, Sr, Ba, Pb) and B = Mn have recently been subject to intense studies owing to the findings of colossal magnetoresistance.[1,2] Phases with different transition metals on B site have also been studied and their magnetoresistive properties have proved to be rather dependent on the chemical nature of B.[2] However, there are still many problems to be solved for the nonsubstituted manganites of the heavy R's. Here we shall address problems related to the crystal and magnetic structure of one particular manganite: metastable, orthorhombic (*o*)$HoMnO_3$.

The stoichiometric manganites $RMnO_3$ (R = La-Lu) can structurally be divided into two different groups. The larger sized R^{3+}'s ($r_{R^{3+}} \geq r_{Dy^{3+}}$) adopt an orthorhombically deformed perovskite-type structure (*Pbnm*), while the smaller R^{3+}'s take a hexagonal structure ($P6_3cm$) which is not related to the atomic arrangements in the perovskite family.[3] However, a perovskite form of the smaller R's can also be prepared by means of special synthesis methods.

The unit-cell dimensions are known for the entire orthorhombic $RMnO_3$ series and indicate an increasing deformation from the ideal perovskite-type arrangement, as R becomes smaller.[4] The perovskite atomic arrangement is characterized by RO_3 close-packed layers, and readjustment of the oxygen atoms is necessary to maintain connections between R^{3+} and O^{2-} when R^{3+} becomes increasingly smaller than O^{2-}. The rearrangement does mainly manifest itself as increasing tilts of the MnO_6 octahedra, which increase the orthorhombic splitting of the unit-cell dimensions compared with the cubic perovskite-type cell.

Positional parameters are available for R = La, Pr, Nd, Tb, Dy, Ho, Y, and Er[5–10] through Rietveld refinements of neutron powder diffraction (NPD) data.

o-$HoMnO_3$ has been synthesized under high pressure[11] and through decomposition of citrate-based precursors.[4,12] Large-scale samples of *o*-$HoMnO_3$ synthesized by the latter procedure are used in this work to examine its crystal and magnetic structure by means of NPD.

The magnetic arrangement of stoichiometric $RMnO_3$ has been reported to be of the antiferromagnetic A type (R = La, Pr, Nd; for nomenclature for magnetic modes see Ref. 13) or the phase is said to be metamagnetic (R = Gd, Tb, Dy, Ho).[5,11,14–17] In addition, a weak ferromagnetic component may be present.[14]

The Néel temperature (T_N) for the ordering of the manganese moments decreases from 141 K for La to 40 K for Tb.[5,15–18] This is in accordance with the trend of decreasing T_N with decreasing R size for the rare earth titanites, vanadites, chromites, and orthoferrites.[15] Ordering of the R moments occurs at a low temperature; below 1.5 K for Pr and Nd,[5] and at 7 K for Tb.[16]

In *o*-$YMnO_3$ the antiferromagnetic arrangement has been reported to be helical, derived from an A mode with $\mathbf{k} = 0.458\mathbf{b}^*$ and $T_N = 42$ K.[19] $TbMnO_3$ has a sinusoidal-wave-type ordering with $\mathbf{k} \approx 0.28\mathbf{b}^*$ below $T_N = 40$ K; above 20 K in an A mode and below 20 K with A and G modes.[16] The ordering of the Tb moments has not yet been completely established, but the arrangement is reported to take a complex short-range ordering with $\mathbf{k} = 0.415\mathbf{b}^*$ and participation of A, C, and G modes.[16]

The magnetic susceptibility of $TbMnO_3$ shows a broad maximum around $T_{Tb} = 7$ K,[16] (Ref. 16 uses the nomenclature T_{N2} for T_{Tb}) and a similar maximum in magnetic susceptibility is seen for *o*-$HoMnO_3$ at 6.5 K.[12]

It is important to understand the physical reasons underlying the complex magnetic behavior of these materials. We have attempted to go a further step in this mission by solving the magnetic structure of *o*-$HoMnO_3$, for which it will be shown that the low-temperature magnetic behavior is far from simple. The remaining part of the paper is organized as

follows. Section II describes the experiments and Sec. III the results and discussion. The crystal structure is considered in Sec. III A and the magnetic ordering temperatures in Sec. III B. Symmetry analyses are reported in Sec. III C and the findings are used to determine the orderings of the magnetic moments of Mn^{3+} and Ho^{3+} described in Secs. III D and *F*, respectively. The manganese ordering is discussed in terms of the exchange interactions (Sec. III E) and a comparison with other rare-earth manganites is given in Sec. III G. Conclusions are given in Sec. IV.

II. EXPERIMENT

Ho_2O_3 (Strem Chem., 99.9%; pre-annealed) and $Mn(CH_3COO)_2 \cdot 4H_2O$ (Fluka, 99%; with thermogravimetric determined water content) were dissolved in melted citric acid monohydrate (Riedel de Häen, 99.5%) and water was added. Stepwise heating of the mixture produced in this way were performed up to a final treatment temperature of 900 °C, where crystallization of *o*-$HoMnO_3$ took place in oxygen. For details see Ref. 12.

Two different samples were synthesized. The first (denoted I) consisted of three different specimens (each ~0.6 g), which each were proved to be single-phase *o*-$HoMnO_3$ by x-ray powder diffraction (XPD; Siemens D5000) and then mixed together. The unit-cell dimensions thus obtained were in good agreement both mutually and with earlier literature values.

The second sample (denoted II) was a mixture of six different batches, which XPD (Guinier-Hägg camera) confirmed to be single phase with fully consistent unit-cell dimensions.

The fraction of Mn^{4+} was determined to be 2(1)% by cerimetric titration. This gives $HoMnO_{3.009(5)}$ or more precisely $Ho_{0.997(2)}Mn_{0.997(2)}O_3$.

Magnetic-susceptibility measurements were performed in the temperature range 5–300 K in magnetic fields up to 5.5 T with a superconducting quantum interference device instrument (Magnetic Property Measurement System; Quantum Design); the sample size was approximately 11 mg.

XPD data for sample I was obtained with a Siemens D5000 diffractometer with Cu$K\alpha_1$ radiation, primary monochromator, position sensitive detector (PSD) and Si as internal standard. For sample II a camera with Guinier-Hägg geometry, Cu$K\alpha_1$ radiation, primary monochromator, and Si internal standard was used.

NPD data at 8 and 295 K for sample I were collected with the PUS two-axis diffractometer at the JEEP II reactor, Kjeller. Monochromatized neutrons of wavelength 1.5527 Å were obtained by reflection from Ge (511) and detected by two 20° (in 2θ) PSD banks. Lower temperatures were obtained by means of a Displex system. An instrumental impurity peak, which appears at $2\theta \approx 32°$, was excluded from the data refinement.

NPD data at 2.8 K were collected at the high-resolution powder diffractometer D2B at ILL, Grenoble, France for sample I. Monochromatic neutrons of wavelength 1.5938 Å were obtained by reflection from Ge (335) and detected by 64 ^{3}He counters.

NPD data for sample II were collected in the diffractometer G4.1 (at the reactor Orphée, Saclay, France), that has a position sensitive detector of 800 cells, spanning an angular range of 80° (2θ from 10 to 90°). A wavelength of 2.426 Å was obtained by reflection (002) from pyrolitic graphite. Diffraction patterns were collected every 3 K from 1.4 to 58.0 K. Each data point is separated by 0.1° (in 2θ).

The crystal and magnetic structures were refined by using the Rietveld refinement program FULLPROF98.[20] A pseudo-Voigt profile function was used. Isotropic temperature factors were refined for the different types of atoms, with typical values (in Å^2): $B_{Ho}=0.50$, $B_{Mn}=0.60$, $B_O=0.70$.

III. RESULTS AND DISCUSSION

A. Crystal structure of *o*-$HoMnO_3$

There is no evidence of magnetic order at 295 K (*vide infra*), and the diffraction pattern (Fig. 1) was found to be in full accordance with the assumed $GdFeO_3$-type structure (Fig. 2, here described in the space group *Pbnm*). Rietveld refinement of the crystal structure gave the unit-cell dimensions and positional parameters listed in Table I.

The octahedral coordination of O around Mn is $(2+2)+2$ (Table II) as a result of Jahn-Teller deformation. Ho is surrounded by 8 O, arranged in a deformed square antiprism. The calculated bond valence for Mn and Ho is 3.17 and 2.96, respectively, and the average Mn-O-Mn angle is as low as 144.1°.

Up to quite recently, there have not been enough consistent structural data to establish precisely the Jahn-Teller distortion as a function of the *R* component in the $RMnO_{3.00}$ series. The data for $LaMnO_{3.00}$ (Refs. 8 and 9) and *o*-$HoMnO_3$ as well as relatively old data for $PrMnO_3$, $NdMnO_3$, and $TbMnO_3$ (Ref. 5) gave a hint about the development in the size of the distortion. The structure data for the three latter phases are mutually consistent and indicate an increasing difference between the two longest and the average of the four shortest Mn-O distances. However, this is not compatible with the findings for $R=$La and Ho. In this situation it was therefore a relief to see the results of the recent room-temperature NPD study[10] of the series with $R=$La, Pr, Nd, Tb, Dy, Ho, Y, and Er (which are reasonably compatible with the mentioned findings for $R=$La, Nd, and Ho, but certainly not with those for $R=$Pr and Tb). Thus it seems established that the Jahn-Teller deformation increases with decreasing R^{3+} size and the consequent increasing tilts of the MnO_6 octahedra. However, the size of the deformation appears to go through a broad maximum around $R=$Dy.

Apart from the thermal expansion in the unit-cell dimensions (Fig. 3 and Table I), there is no evidence of distinct alterations in the crystal structure of *o*-$HoMnO_3$ between 2.8 and 295 K. It is, in particular, worth noting that the passages of the magnetic ordering temperatures for the Mn^{3+} and Ho^{3+} sublattices (*vide infra*) have virtually no impact on the variables of the crystal structure.

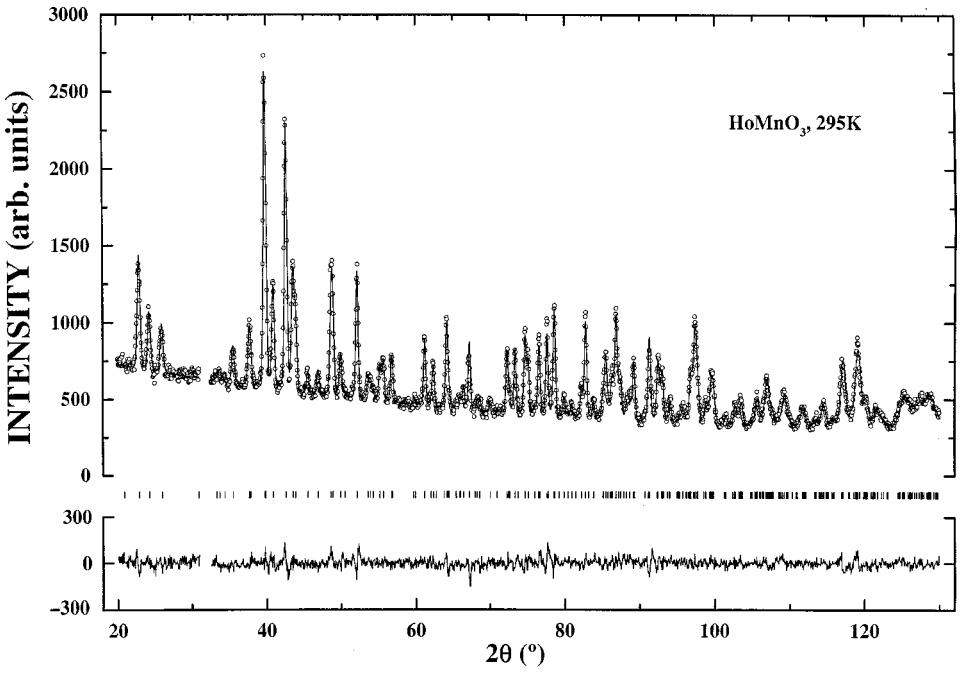

FIG. 1. Rietveld refinements (upper line) of NPD data collected with PUS (circles) for o-$HoMnO_3$ at 295 K. Positions of Bragg reflections (nuclear contributions) are shown with bars. The difference between observed and calculated intensity is shown with the bottom line.

B. Néel temperature

At low temperature several extra reflections, originating from cooperative magnetism, are revealed in the NPD patterns. The strongest magnetic reflection (which later will be recognized as $001^{\pm}$) and its weaker neighbor (011^{-}) is shown as a function of temperature in Fig. 4. Two different magnetic ordering schemes are immediately recognized; one between ca. 36 and 13 K and the other below ca. 13 K, the latter with higher intensity. From the trend in the magnetic properties of the $R$$MnO_3$ perovskites it is reasonable to conclude that the magnetic moments of manganese order (approaching saturation near 13 K) in the highest temperature interval, while the holmium moments order at lower tem-

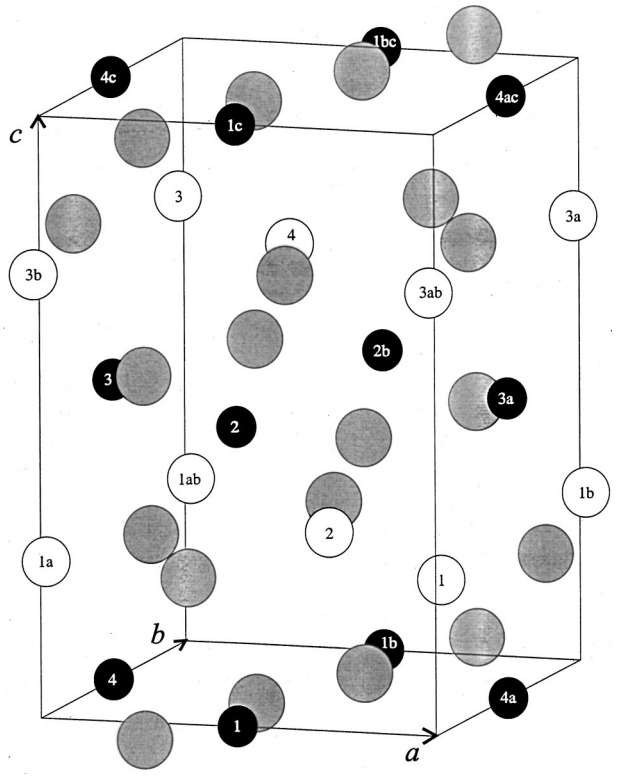

FIG. 2. The $GdFeO_3$-type crystal structure of o-$HoMnO_3$ (see Table I); Ho^{3+} (open circles), Mn^{3+} (black circles), and O^{2-} (shaded circles). The numbering of the Ho^{3+} and Mn^{3+} atoms refers to the magnetic arrangement.

TABLE I. Crystal and magnetic structure parameters for o-$HoMnO_3$ according to Rietveld refinements of NPD data. This description is based on space group *Pbnm* with Ho in 4*c*, Mn in 4*b*; O1 in 4*c*, and O2 in 8*d*.

T (K)	295 (PUS)	8 (PUS)	2.8 (D2B)
a (Å)	5.2549(2)	5.2481(2)	5.24765(10)
b (Å)	5.8263(2)	5.8188(2)	5.81744(11)
c (Å)	7.3648(3)	7.3431(3)	7.3447(2)
x_{Ho}	0.9832(5)	0.9833(5)	0.9830(4)
y_{Ho}	0.0848(3)	0.0850(3)	0.0836(3)
x_{O1}	0.3902(5)	0.3895(5)	0.3894(5)
y_{O1}	−0.0368(5)	−0.0355(5)	−0.0369(4)
x_{O2}	0.7014(4)	0.7007(4)	0.6999(3)
y_{O2}	0.3261(4)	0.3264(4)	0.3275(3)
z_{O2}	0.0529(3)	0.0533(3)	0.0533(2)
$\mu_{AF,Mn}(\mu_B)$		3.96	3.96
$\mu_{AF,Ho}(\mu_B)$		4.85(10)	7.65(9)[a]
k/**b***		0.4289(11)	0.4263(5)
R_{nucl} (%)	3.59	4.02	3.64
R_{mag} (%)		12.1	7.26
χ^2	1.22	1.76	1.75

[a]The G4.1 data gave 7.69(5) μ_B at 1.4 K.

TABLE II. Selected distances (in Å) and angles (degrees) from Rietveld refinements of NPD data of o-$HoMnO_3$. Estimated standard deviation of the distances is 5–8 in the last digit.

T (K)	295	8	2.8
Mn-O1(×2)	1.907	1.907	1.908
Mn-O2(×2)	1.940	1.935	1.937
Mn-O2(×2)	2.206	2.206	2.210
$\overline{d}_{\text{Mn-O}}$	2.018	2.018	2.018
Ho-O1(×1)	2.252	2.243	2.246
Ho-O1(×1)	2.299	2.306	2.306
Ho-O1(×1)	3.193	3.139	3.192
Ho-O1(×1)	3.681	3.670	3.671
Ho-O2(×2)	2.306	2.297	2.287
Ho-O2(×2)	2.501	2.501	2.513
Ho-O2(×2)	2.559	2.554	2.552
Ho-O2(×2)	3.664	3.665	3.669
$\overline{d}_{\text{Ho-O}}$	2.410	2.407	2.407
Mn-O2-Mn(×4)	144.6	144.3	144.0
Mn-O1-Mn(×2)	142.9	142.9	142.9

perature. By plotting the peak intensities against temperature, T_N could be determined to be close to 40 K and T_{Ho} near 15 K (left inset to Fig. 5). A more accurate approach for determination of T_N is to plot the reduced magnetic moment (obtained by Rietveld refinements) against T/T_N for different T_N and make comparison with the Brillouin function for $J=S=2$, corresponding to Mn^{3+}. The best fit is obtained by using $T_N=38$ K (Fig. 5). T_{Ho} could not be determined accurately by this method, but the best fit to the Brillouin function for $J=4$ (corresponding to Ho^{3+}) was obtained with $T_{\text{Ho}}=11$ K (right inset to Fig. 5). This is supported by the fact that the deviation from the Curie-Weiss law (dominated by the Ho^{3+} moments) starts at 11.0 ± 0.5 K (Fig. 6).

The magnetic ordering of manganese is not revealed in the susceptibility curve of o-$HoMnO_3$. The same appears to be the case for several other members of the $RMnO_3$ series where R^{3+} carries a large magnetic moment.[11,14,15] Nevertheless, the trend of decreasing T_N with decreasing size of R^{3+} is well established from NPD data.[5,15–18] The explanation for this size dependence is related to the structural change in the e_g^1-$2p_\sigma$-e_g^1 and t_{2g}^3-$2p_\pi$-t_{2g}^3 superexchange paths.[21] As R^{3+} becomes smaller, the MnO_6 octahedra turn more in the tilting process and the Mn-O-Mn angle decreases [average angle for o-$HoMnO_3$ is 144° compared to 155° for $LaMnO_3$ (Refs. 8–10)], thus weakening the superexchange interaction and decreasing T_N. The splitting of the unit-cell parameters of an adopted pseudocubic $2\times2\times2$ perovskite cell (an indicator of the Mn-O-Mn angle; Fig. 7) levels out with the decreasing size of R^{3+} when the stability limit of the $GdFeO_3$-type arrangement is approached,[4] and this could explain the minor variation in T_N for the larger R^{3+}'s.

T_R seems to have the opposite dependence on the size of R^{3+}, but the actual ordering temperatures are generally very low and the values more scattered. The role of the crystal-field effects is very important in the magnetic anisotropy of R^{3+} and this may influence the ordering temperature for the R sublattices. Hence, the safest is to maintain that T_R is independent of the size of R^{3+}.

For a $TbMnO_3$ single-crystal, neutron diffraction proved T_{Tb} to be 7 K, where the magnetic susceptibility is found to exhibit a maximum.[16] For o-$HoMnO_3$, T_{Ho} is slightly higher than the temperature of the maximum in magnetic susceptibility. In fact, the behavior of the magnetic susceptibility for a perovskite with magnetic ions on both A and B sites and a large number of different exchange interactions is very difficult to predict.

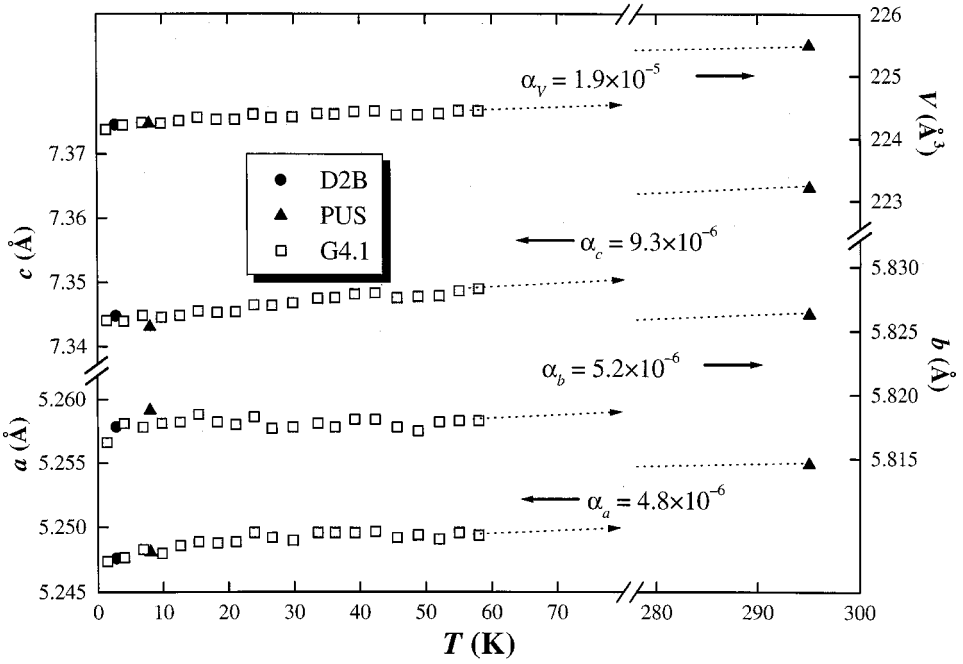

FIG. 3. Thermal-expansion data for o-$HoMnO_3$ between 2.8 and 295 K. Numerical values for the linear expansion coefficients are given on the illustration.

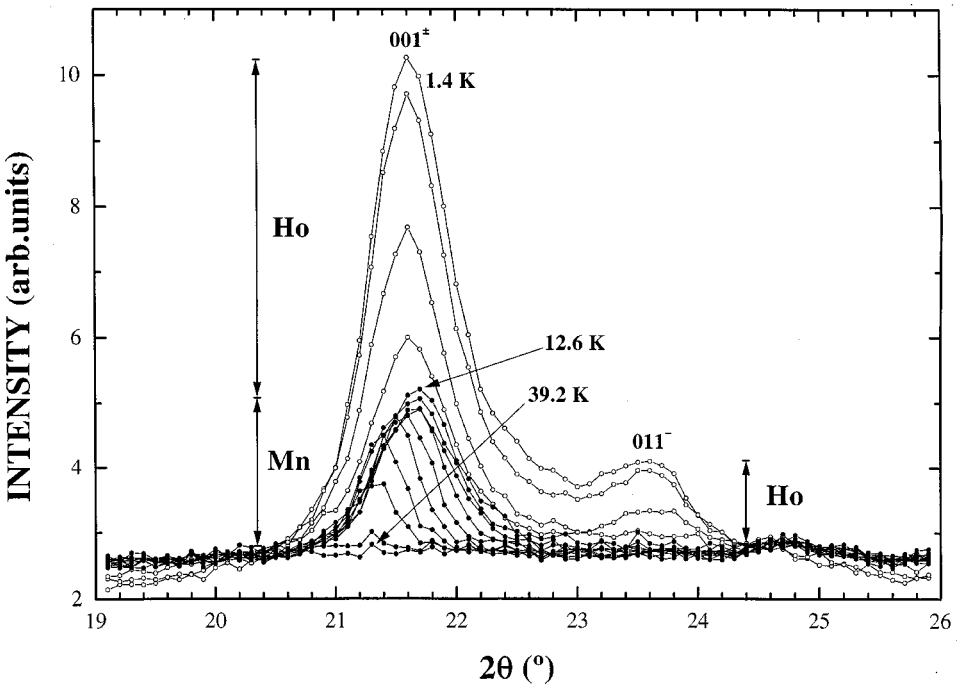

FIG. 4. NPD data collected with G4.1 for o-$HoMnO_3$. The strongest magnetic peak $001^{\pm}$ and its neighbor 011^{-} are shown below (open circles) and above (filled circles) T_{Ho}. The temperature difference between each of these recordings is approximately 3 K.

C. Symmetry analysis

In order to determine the magnetic structure of the Mn^{3+} and R^{3+} sites in $RMnO_3$ perovskites it is very important to classify the possible spin configurations according to the irreducible representations (ireps) of the space group for the propagation vector. For o-$HoMnO_3$, all the magnetic reflections can be indexed using a propagation vector $\mathbf{k}=k_y\mathbf{b}^*$ with $k_y \leqslant \frac{1}{2}$. Symmetry analysis for space group *Pbnm* with this kind of propagation vector has earlier been performed for the $4b$ position, obtaining the different basis functions of the ireps describing the magnetic ordering at this site.[22] We have extended this analysis for all magnetic sites and the final results are summarized in Table III.

The decomposition of the full reducible magnetic representation Γ (of dimension 3 times the number of atoms in the primitive cell) for $4b$ is: $\Gamma_{4b}=\Sigma_{\oplus} n_\nu \Gamma_\nu = 3\Gamma_1 \oplus 3\Gamma_2 \oplus 3\Gamma_3 \oplus 3\Gamma_4$, the corresponding decomposition for the two $4c$ sites is: $\Gamma_{4c1,4c2}=\Gamma_1 \oplus 2\Gamma_2 \oplus \Gamma_3 \oplus 2\Gamma_4$. The number of free parameters for a magnetic structure corresponding to an irep is equal to the product ($n_{\text{free}}=n_\nu d_\nu$) of the number of times (n_ν) the irep Γ_ν is contained in Γ and the dimension (d_ν) of the irep. This is also the total number of independent basis function vectors.

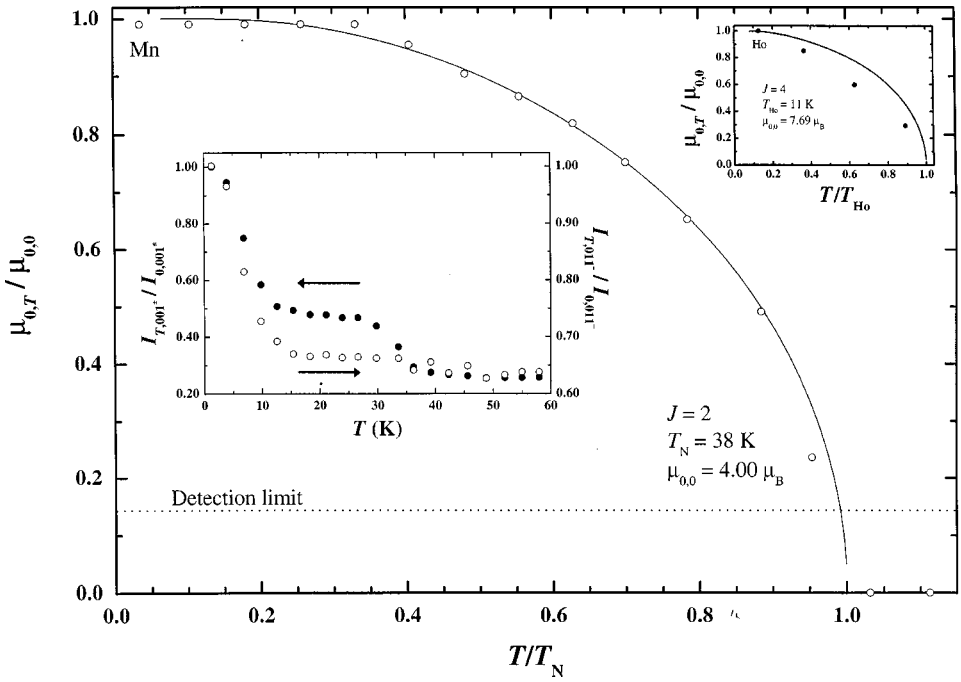

FIG. 5. Reduced magnetic moment of Mn^{3+} as a function of reduced temperature compared to the Brillouin function for $J=S=2$ and $T_N=38$ K. Right inset: Reduced magnetic moment of Ho^{3+} as a function of reduced temperature compared to the Brillouin function for $J=4$ and $T_{Ho}=11$ K. Left inset: Reduced intensity of the magnetic reflections $001^{\pm}$ and 011^{-} as a function of temperature (see Fig. 4).

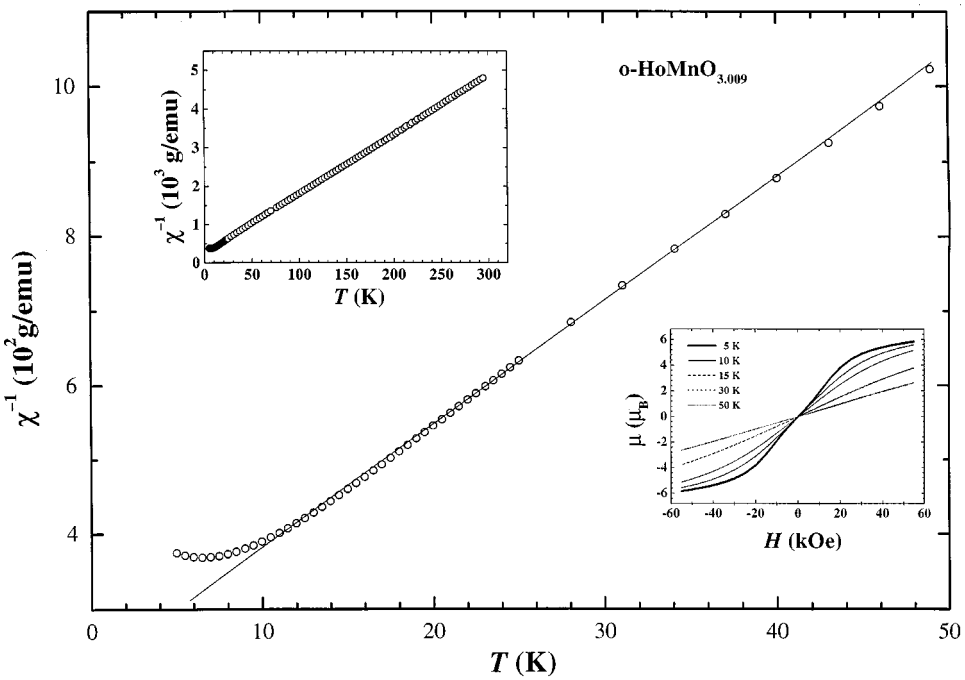

FIG. 6. Inverse susceptibility vs temperature; onset of deviations from Curie-Weiss law at 11.0±0.5 K. Left inset: The entire inverse susceptibility characteristic below room temperature. Right inset: Magnetic moment as a function of magnetic field at 5, 10, 15, 30, and 50 K.

The magnetic moment of the atom ''*j*'', in the cell with origin at the lattice point $\mathbf{R}_n$, in a magnetic structure characterized by the set of propagation vectors $\{\mathbf{k}\}$, is given by the Fourier series: $\mathbf{m}_{nj}=\sum_{\{\mathbf{k}\}}\mathbf{S}_{\mathbf{k}j}\cdot e^{-2\pi i\mathbf{k}\cdot\mathbf{R}_n}$, where the sum is extended to the whole set of propagation vectors. For $\mathbf{k}$ at the interior of the Brillouin zone the vector $-\mathbf{k}$ should also be present and $\mathbf{S}_{\mathbf{k}j}=\mathbf{S}^*_{-\mathbf{k}j}$. The physical meaning of the basis functions of the irep Γ_ν in describing a magnetic structure is that the Fourier coefficients $\mathbf{S}_{\mathbf{k}j}$ are linear combinations of the constant vectors $\mathbf{S}_\alpha(\mathbf{k},\upsilon,\lambda|j)$, so that

$$\mathbf{S}_{\mathbf{k}j}=\Sigma_{\alpha\lambda}C_{\alpha\lambda}\mathbf{S}_\alpha(\mathbf{k},\nu,\lambda|j).$$

For a given propagation vector $\mathbf{k}$ and a given irep Γ_ν, the index α runs between 1 and n_ν and λ between 1 and d_ν (for details, see Ref. 23). The coefficients $C_{\alpha\lambda}$ can be real or purely imaginary. By varying these coefficients we obtain the whole class of magnetic structures satisfying the symmetry of the propagation vector. Let us consider two examples for the manganese sublattices constructed with the representation Γ_3. The irep is of dimension 1 (so $\lambda=1$ and the summation index over λ is therefore removed) and it is contained 3 times in Γ_{4b}, so the number of coefficients is 3 ($\alpha=1$, 2, 3). The possible magnetic structures described by this irep are given by

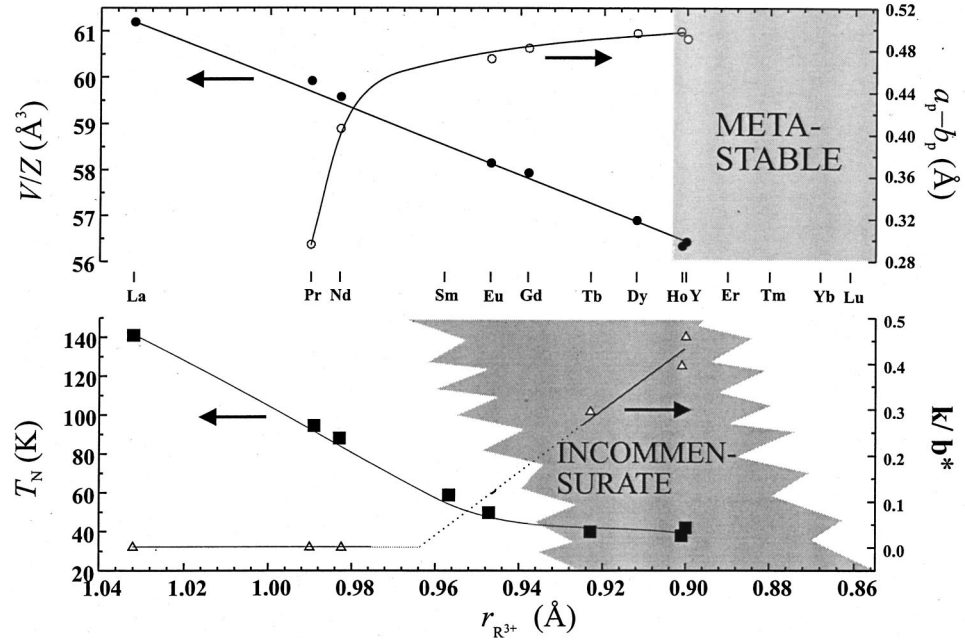

FIG. 7. Structural (top: unit-cell volume V/Z; deviation from cubic, a_p-b_p, for an adapted pseudocubic $2\times2\times2$ perovskite unit cell, see Ref. 4) and magnetic (bottom: T_N; $\mathbf{k}/\mathbf{b}^*=k_y$, *vide infra*) characteristics for $R\mathrm{MnO_3}$ as function of $r_{R^{3+}}$. Literature data are taken from Refs. 4, 5, 8, 15–17, and 19.

TABLE III. Irreducible representations (ireps) for the group of the propagation vector $\mathbf{G_k}\,\mathbf{k}=k_y\mathbf{b}^*$ ($k_y<\frac{1}{2}$) in the space group *Pbnm*. For $\mathbf{G_k}=Pb2_1m$ the center of symmetry is lost. The coset representatives of $\mathbf{G_k}$ are $\{1,m_z,2_{1y},b_x\}=\{(x,y,z),(x,y,-z+\frac{1}{2}),(-x+\frac{1}{2},y+\frac{1}{2},-z+\frac{1}{2}),(-x+\frac{1}{2},y+\frac{1}{2},z)\}$. There are four one-dimensional irreducible representations. The basis functions of positions 4*b* and 4*c* are also given. We have used an extension to complex basis functions with the Bertaut (Ref. 13) notations for the modes *F*, *A*, *C*, *G*. The value of ω is $e^{i\pi k_y}$. The numbering of atoms in the 4*b* site is: $\mathrm{Mn}_1(\frac{1}{2},0,0)$, $\mathrm{Mn}_2(\frac{1}{2},0,\frac{1}{2})$, $\mathrm{Mn}_3(0,\frac{1}{2},\frac{1}{2})$, $\mathrm{Mn}_4(0,\frac{1}{2},0)$. The atoms in the 4*c* site split in two orbits (previously related by the center of symmetry) having the same basis functions. The coupling between these two orbits is usually positive or negative, but in the general case there is a phase factor between them. The holmium atoms of the first orbit are: $\mathrm{Ho}_1(x,y,\frac{1}{4})$, $\mathrm{Ho}_4(1\frac{1}{2}-x,y+\frac{1}{2},\frac{1}{4})$, and those of the second orbit: $\mathrm{Ho}_2(1-x,1-y,\frac{3}{4})$, $\mathrm{Ho}_3(x-\frac{1}{2},\frac{1}{2}-y,\frac{3}{4})$, with $x\approx0.985$ and $y\approx0.085$. The symbols (*f*,*a*) used to describe the basis functions for the Ho orbits correspond to *F* and *A* for a two-atoms orbit.

					Basis functions vectors $\mathbf{S}(\mathbf{k},\nu,\lambda\|j)$ for 4*b* site					Basis functions vectors $\mathbf{S}(\mathbf{k},\nu,\lambda\|j)$ for two 4*c* orbits				
Γ_ν	1	m_z	2_{1y}	b_x	Mn_1	Mn_2	Mn_3	Mn_4		Ho_1	Ho_4		Ho_2	Ho_3	
Γ_1	1	1	ω	ω	(100)	(-100)	$(-\omega00)$	$(\omega00)$	A_x						
					(010)	$(0-10)$	$(0\omega0)$	$(0-\omega0)$	G_y						
					(001)	(001)	$(00-\omega)$	$(00-\omega)$	C_z	(001)	$(00-\omega)$	a_z	(001)	$(00-\omega)$	a_z
Γ_2	1	-1	ω	$-\omega$	(100)	(100)	$(-\omega00)$	$(-\omega00)$	C_x	(100)	$(-\omega00)$	a_x	(100)	$(-\omega00)$	a_x
					(010)	(010)	$(0\omega0)$	$(0\omega0)$	F_y	(010)	$(0\omega0)$	f_y	(010)	$(0\omega0)$	f_y
					(001)	$(00-1)$	$(00-\omega)$	(00ω)	A_z						
Γ_3	1	1	$-\omega$	$-\omega$	(100)	(-100)	$(\omega00)$	$(-\omega00)$	G_x						
					(010)	$(0-10)$	$(0-\omega0)$	$(0\omega0)$	A_y						
					(001)	(001)	(00ω)	(00ω)	F_z	(001)	(00ω)	f_z	(001)	(00ω)	f_z
Γ_4	1	-1	$-\omega$	ω	(100)	(100)	$(\omega00)$	$(\omega00)$	F_x	(100)	$(\omega00)$	f_x	(100)	$(\omega00)$	f_x
					(010)	(010)	$(0-\omega0)$	$(0-\omega0)$	C_y	(010)	$(0-\omega0)$	a_y	(010)	$(0-\omega0)$	a_y
					(001)	$(00-1)$	(00ω)	$(00-\omega)$	G_z						

$$\mathbf{S}_{\mathbf{k}1}=\mathbf{\Sigma}_\alpha C_\alpha \mathbf{S}_\alpha(\mathbf{k},\nu,1|1)=C_1(1,0,0)+C_2(0,1,0)+C_3(0,0,1)$$

$$=(C_1,C_2,C_3)$$

$$\mathbf{S}_{\mathbf{k}2}=\mathbf{\Sigma}_\alpha C_\alpha \mathbf{S}_\alpha(\mathbf{k},\nu,1|2)$$

$$=C_1(-1,0,0)+C_2(0,-1,0)+C_3(0,0,1)$$

$$=(-C_1,-C_2,C_3)$$

$$\mathbf{S}_{\mathbf{k}3}=\mathbf{\Sigma}_\alpha C_\alpha \mathbf{S}_\alpha(\mathbf{k},\nu,1|3)$$

$$=C_1(\omega,0,0)+C_2(0,-\omega,0)+C_3(0,0,\omega)$$

$$=\omega(C_1,-C_2,C_3)$$

$$\mathbf{S}_{\mathbf{k}4}=\mathbf{\Sigma}_\alpha C_\alpha \mathbf{S}_\alpha(\mathbf{k},\nu,1|4)$$

$$=C_1(-\omega,0,0)+C_2(0,\omega,0)+C_3(0,0,\omega)$$

$$=\omega(-C_1,C_2,C_3).$$

If, e.g., $C_1=C_3=0$, the structure corresponds to a collinear longitudinal sinusoidal structure. If $C_2=0$, and $C_1=iC_3$ with C_3 purely imaginary, the structure corresponds to a helix with a cylindrical envelope. If $C_1=0$ and $C_2=iC_3$ the structure is a cycloid, etc.

To solve the magnetic structure one has to look for the set of coefficients that give rise to the best agreement between observed and calculated magnetic intensities. This part of the analysis may be undertaken just by trial and error by hand or using Monte Carlo techniques.

D. Magnetic ordering of Mn^{3+}

Just below T_N the magnetic reflections can be indexed with a propagation vector nearly equal to the propagation vector for *o*-$YMnO_3$. Depending on temperature, **k** varies in the region $0.395\mathbf{b}^*$ to $0.431\mathbf{b}^*$ (inset to Fig. 8). Susceptibility measurements (Fig. 6) show no indication of a ferromagnetic component. This is consistent with the observed **k** vector in the interior, $\mathbf{k}\neq(0,0,0)$, of the Brillouin zone. The fact that manganese is in a special position, allows a simple de-

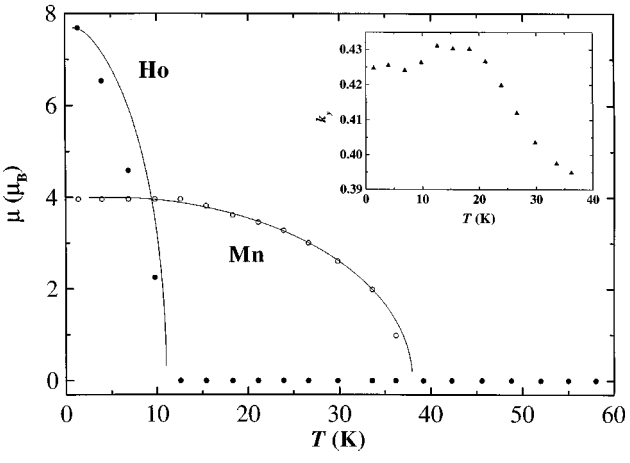

FIG. 8. Magnetic moment amplitudes for *o*-$HoMnO_3$ refined from NPD data obtained with G4.1 as a function of temperature for Ho^{3+} (filled circles) and Mn^{3+} (open circles) compared with Brillouin functions (lines). Inset: Magnitude of propagation vector k_y as a function of temperature.

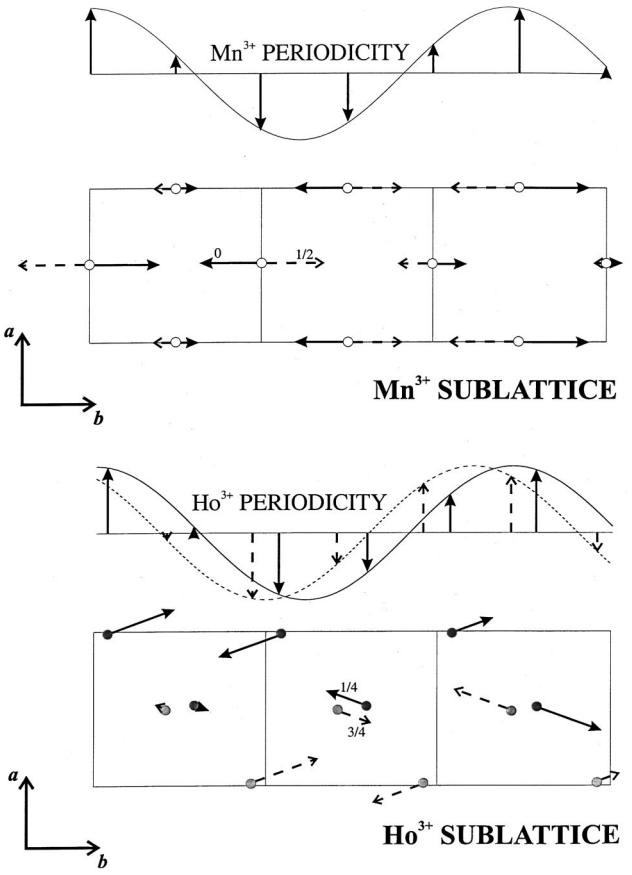

FIG. 9. The magnetic arrangement in o-$HoMnO_3$. Top: Ordering of the magnetic moments of Mn in the *ab* plane for three crystallographic unit cells. The sinusoidal modulation of the magnetic moments is also shown. Bottom: Ordering of the magnetic moments of Ho^{3+} in the *ab* plane with corresponding sinusoidal modulation of the moments for the two different orbits. Note that at a given temperature, there is only one common propagation vector, but there may be phase differences between the three magnetic sites.

termination of the magnetic structure from the extinction rules of the satellites as deduced from the expression of the magnetic structure factor. The observed satellites verify that the parent reflections (hkl) satisfy $h+k=2n$ and $l=2n+1$. Hence only pure A modes are compatible with these observations in the temperature range 13–36 K. Other possible modes present in the magnetic structure are below the detection limit of the present experiments. Then, there are three possibilities left: $\Gamma_1(A_x00)$, $\Gamma_2(00A_z)$, and $\Gamma_3(0A_y0)$ if the magnetic structure is described by a single irep. The mixing of ireps is also possible, so modes of the form $\Gamma_1 \oplus \Gamma_2(A_x0A_z)$ or even $\Gamma_1 \oplus \Gamma_2 \oplus \Gamma_3(A_xA_yA_z)$ are conceivable.[23] The first three alternatives correspond to sinusoidal structures (transverse for Γ_1 and Γ_2 and longitudinal for Γ_3) and the mixing of ireps offers the possibility of having helical, cycloidal, or sinusoidal orderings. Rietveld refinements of $\Gamma_1(A_x00)$ and $\Gamma_2(00A_z)$ with a magnetic moment perpendicular to the propagation vector inevitably resulted in enhanced calculated intensity for several reflections, while $\Gamma_3(0A_y0)$, e.g., $C_1=C_3=0$ and $C_2\neq 0$, gave a fully satisfactory fit. Hence the moments of Mn^{3+} order with

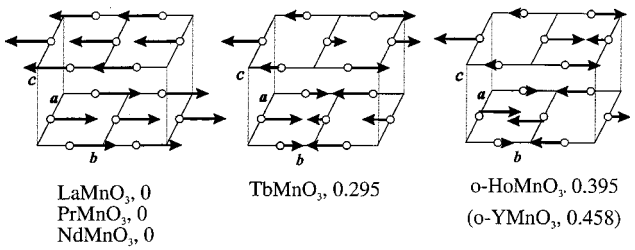

FIG. 10. The magnetic ordering of Mn^{3+} in $RMnO_3$ [R=La, Pr, Nd, Tb, Ho (and Y)] in two adjacent *ab* slabs. The numerical values refer to the periodicity just below T_N.

the magnetic moment modulated in a longitudinal sinusoidal wave along the propagation vector. This ordering is visualized in Fig. 9 and compared to the magnetic arrangement in $LaMnO_3$ and $TbMnO_3$ in Fig. 10.

The amplitude of the magnetic moment was refined for the G4.1 data at all available temperatures. The nuclear structure and isotropic temperature factors were kept constant and equal to the refined D2B data at 2.8 K. Special care was taken to select the correct background position around the largest magnetic peaks because the determination of the moment is fairly sensitive to this. Below T_{Ho} the moment of Mn^{3+} was kept constant in order to stabilize the refinements (see Sec. III F). The thus derived magnetic structure parameters are listed in Table I and illustrated in Figs. 8–10.

E. Exchange interactions

The occurrence of a sinusoidal magnetic structure as the first magnetic ordered state for manganese in o-$HoMnO_3$ is the consequence of the competition between magnetic interactions which gives rise to a certain degree of frustration. An analysis of the exchange integrals has been partially performed in Ref. 19. The first magnetic ordered state corresponds to the maximum eigenvalue for the Fourier transform Hermitian matrix of the exchange integrals (see Ref. 24, but note that we use a different sign convention: here a negative exchange integral corresponds to antiferromagnetic coupling, the magnetic energy of a pair is given by $E_{ij}=-J_{ij}\mathbf{S}_i\cdot\mathbf{S}_j$):

$$\xi_{ij}(\mathbf{k})=\Sigma_n J_{ij}(\mathbf{R}_n)\cdot e^{-2\pi i\mathbf{k}\cdot\mathbf{R}_n},$$

where the index pair ij refers to a particular numbering of atoms within a primitive cell so that $J_{ij}(\mathbf{R}_n)$ is the exchange integral between an atom i in the reference (origin) cell and an atom j in the cell with origin at $\mathbf{R}_n$. If only isotropic exchange interactions are considered, the magnetic structure is degenerated with respect to a complete rotation of all the spins in the crystal. The eigenvectors of $\xi_{ij}(\mathbf{k})$ are the modes that may be combined to construct general helical structures. A list of exchange interactions that may be considered as contributing to determine the magnetic structure of o-$HoMnO_3$ is given in Table IV.

The problem of the ground state is too complicated to be treated here, however, we can make some simplifications in order to get some insight into the conditions which must be satisfied by the exchange integrals in order to arrive at the first ordered magnetic state of Mn. The 4×4 matrix $\xi_{ij}(\mathbf{k})$

TABLE IV. Exchange paths possibly contributing to determine the magnetic ground state of o-$HoMnO_3$ (*Pbnm* setting). The numbering of atoms is as in Table III. A lattice translation has been added to appropriate second atoms in order to identify representative pairs for each exchange integral. The notations for the Mn-Mn (MM) exchange integrals are the same as in Ref. 19; MH is used for Mn-Ho interactions, and HH for Ho-Ho interactions.

Exchange integral	Representative atom pair	Number of equivalents	Separation (in Å) at 2.8 K	Exchange path via oxygen
J_{12}	Mn_1-Mn_2	2	3.672	MM superexchange
J_{14}	Mn_1-Mn_4	4	3.917	MM superexchange
J_{11a}	Mn_1-$Mn_1(100)$	2	5.248	MM super-superexchange
J_{11b}	Mn_1-$Mn_1(010)$	2	5.818	MM super-superexchange
J_{13}	Mn_1-Mn_3	8	5.370	MM super-superexchange
J_{MR1}	Mn_1-$Ho_2(0\bar{1}0)$;$Ho_4(00\bar{1})$	2	3.036	MH superexchange
J_{MR2}	Mn_1-Ho_1;$Ho_3(0\bar{1}\bar{1})$	2	3.178	MH superexchange
J_{MR3}	Mn_1-$Ho_1(\bar{1}00)$;$Ho_3(\bar{1}1\bar{1})$	2	3.303	MH superexchange
J_{MR4}	Mn_1-Ho_2;$Ho_4(0\bar{1}1)$	2	3.865	MH superexchange
J_{RR1}	Ho_1-$Ho_3(1\bar{1}0)$	2	3.805	HH superexchange
J_{RR2}	Ho_1-Ho_2	2	3.816	HH superexchange
J_{RR3}	Ho_1-$Ho_2(100)$	2	4.022	HH superexchange

for the Mn sublattices (see Figs. 2, 9, and 10) can be easily constructed for the exchange integrals of Table IV. This matrix has been discussed in detail by Bertaut[13] and applied to the case of o-$YMnO_3$.[19] As discussed by these authors the eigenvalue corresponding to the A mode, along the direction $\mathbf{k}=k_y\mathbf{b}^*$, can be written as

$$\lambda_A(0,k_y,0)=2(J_{11a}-J_{12})+2J_{11b}\cos(2\pi k_y)-4(2J_{13}-J_{14})\cos(\pi k_y).$$

The derivative of λ_A with respect to k_y

$$\partial\lambda_A/\partial k_y=4\pi\sin(\pi k_y)[-2J_{11b}\cos(\pi k_y)+2J_{13}-J_{14}]=0$$

should be zero for a maximum.

The condition for the mode A being more stable than the G mode is: $2J_{13}-J_{14}<0$.[19] Provided this condition is fulfilled, λ_A is at maximum for $k_y=0$ or for $\cos(\pi k_y)=(2J_{13}-J_{14})/(2J_{11b})$. The first solution corresponds to the antiferromagnetic magnetic structure observed for $LaMnO_3$, whereas the second solution gives rise to either a sinusoidal or an helical structure (the magnetic isotropic energy is degenerate), depending on whether we consider constant magnetic moments or not. Considering $\mathbf{k}$ at the interior of the Brillouin zone, the second solution gives as a strong condition for the exchange interactions the relation: $0<(2J_{13}-J_{14})/(2J_{11b})<1$.

There are two exchange integrals, J_{13} and J_{14}, which determine the mode (A or G) and three (J_{13}, J_{14} and J_{11b}) which determine k_y (see Ref. 19). The nearest-neighbor interaction between Mn_1 and Mn_2 does not have any influence on this. From the equations above it follow that J_{11b} is negative. The strong Jahn-Teller effect in o-$HoMnO_3$ implies that J_{14} is positive and certainly greater than the super-superexchange interactions J_{13} and J_{11b} that should be of the same order of magnitude. The fact that k_y increases from $TbMnO_3$ to o-$HoMnO_3$ means that $(2J_{13}-J_{14})/(2J_{11b})$ decreases. This could be due to decreasing J_{14} caused by decreasing Mn-O-Mn angle (see also Ref. 25).

In order to go further into the origin of the incommensurate magnetic structure of o-$HoMnO_3$ it is necessary to get more insight into the mutual signs and magnitudes of J_{13}, J_{14}, and J_{11b}. In the anticipation of theoretical electronic band-structure based calculations, it has been attempted to extract interaction information from the available crystal structure data. An obvious approach is to try to relate the tilt characteristics of $GdFeO_3$-type manganites to the magnetic interactions concerned. The relationship between the adapted deformation indicator (a_p-b_p) and $\mathbf{k}/\mathbf{b}^*=k_y$ in Fig. 7 suggests that interesting information may be hidden here. However, the problem is that there are two different tilt angles, α and β, involved,

$$a_p-b_p=2a_0\cos\alpha(\cos\alpha-\cos\beta),$$

where a_0 refers to perovskite aristotype cell. In addition comes the deformation of MnO_6 octahedra themselves. Hence the relevant angles and distances for the exchange paths become complicated expressions of the actual deformations. Furthermore, it appears to be no simple relations between angles and distances on the one hand and exchange interactions on the other.

In this situation we limit our concluding considerations on this aspect to the use of the qualitative predictions of the Kanamori-Goodenough superexchange rules.[26] This predicts ferromagnetism in the ab plane for 180° Mn-O-Mn interaction, due to the Jahn-Teller effect and the antiferrodistortional orbital ordering, and antiferromagnetism along the c axis for nearest-neighbors interactions (as observed for $LaMnO_3$).[26] For an intermediate range of angles a competition between ferromagnetic ($d^1_{z^2}$-$2p_\sigma$-$d^0_{x^2-y^2}$) and antiferromagnetic (t^3_{2g}-$2p_\pi$-t^3_{2g}) interactions in the ab plane may re-

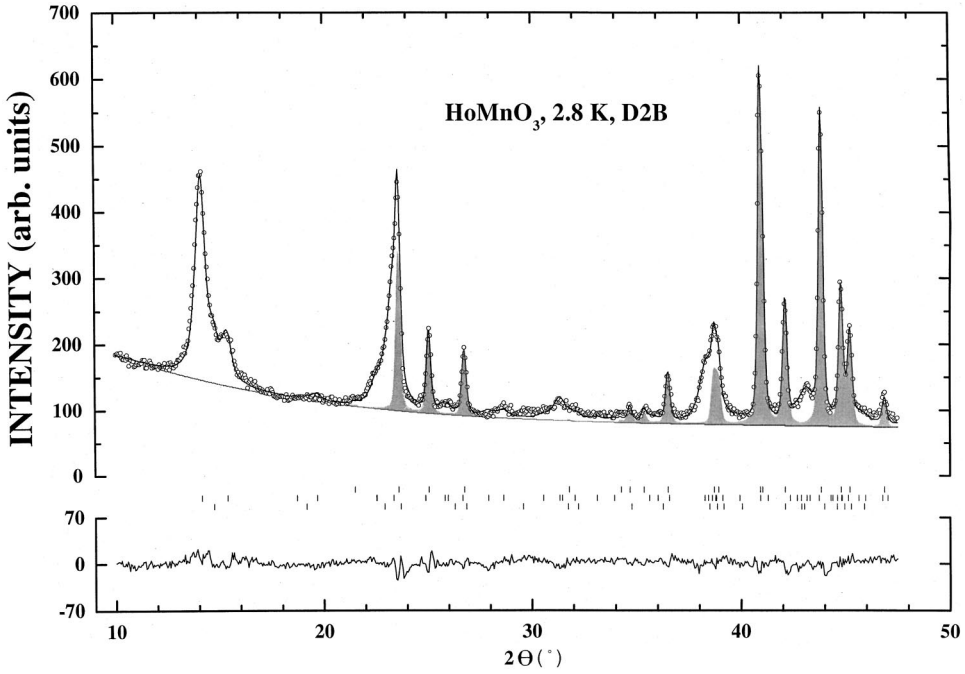

FIG. 11. Rietveld refinements (upper line) of NPD data collected with D2B (circles) for o-$HoMnO_3$ at 2.8 K ($\lambda = 1.5938$ Å). Simulated nuclear contribution is shaded. Positions of Bragg reflections are shown with bars for the nuclear (upper) and magnetic (incommensurate in middle; commensurate at bottom) contribution. The difference between observed and calculated intensity is shown with the bottom line.

sult in weakening of the effective in-plane Mn-O-Mn nearest-neighbors interactions. Next-nearest-neighbor interactions become competitive and a delicate balance may produce a complex magnetic behavior. In the o-$HoMnO_3$ case the overall frustration obviously results in a sinusoidal wave as the first-ordered state for Mn^{3+}. For the particular value of $k_y = 0.395$ obtained just below T_N, the condition $\cos(\pi k_y) = (2J_{13} - J_{14})/(2J_{11b})$ gives: $J_{14} \approx 2(J_{13} - 0.324 J_{11b})$, which is positive. Hence with the assumption of negative super-superexchange interactions J_{13} and J_{11b}, the (strong) condition becomes: $0.324|J_{11b}| > |J_{13}|$.

F. Magnetic ordering of Ho^{3+}

The different possible magnetic modes for the holmium site did not give intensity contribution to easily recognizable groups of reflections. Hence in order to solve the Ho^{3+} magnetic structure and establish a good starting model for the Rietveld refinements a Monte Carlo search by means of the integrated intensities was necessary. The Mn^{3+} moment was kept constant and the different representations for Ho^{3+} examined. This clearly showed that a Γ_2 description for Ho^{3+} represents the best solution. Monte Carlo searches with Mn^{3+} in other representations instead did not improve the fit.

With both Ho^{3+} orbits ordering in $\Gamma_2(a_x, f_y, 0)$ and Mn^{3+} in $\Gamma_3(0, A_y, 0)$ the complete magnetic structure could in principle be similar [i.e., $(G_x, A_y, 0)$] for both kinds of magnetic atoms. The obtained magnetic arrangement of Ho^{3+} is illustrated in Fig. 9 and the plot of the Rietveld refinements to the complete nuclear and magnetic structure of o-$HoMnO_3$ at 2.8 K in Fig. 11. There is a phase difference between the two Ho^{3+} orbits of $\sim 34°$. A phase difference of 26° would have made the spin amplitude of neighboring Ho^{3+} equal, resulting in a global $(G_x, A_y, 0) = (a_x, f_y, 0)_1 + (a_x, -f_y, 0)_2$ ordering (see the projection on the *ab* plane in Fig. 9). The slightly deviating phase difference makes the present description become an approximation. Hence to a very good approximation (Fig. 9) Ho^{3+} is ordered according to $(G_x, A_y, 0)$, whereas a G_x component is definitely absent for Mn^{3+}. The present NPD data were, according to our simulations, rather insensitive to phase differences between the Mn and Ho sites.

In addition to the already considered magnetic contributions from Mn^{3+} and Ho^{3+}, the D2B data contained a small and broad intensity contribution which could be indexed as $(0\ \frac{1}{2}\ 1)$ for the nuclear unit cell. This could be explained as a secondary magnetic phase with a doubled *b* axis. Although the diffraction pattern did not contain enough information to unequivocally solve this structure, a plausible model which is in accordance with NPD would be a modulated commensurate magnetic structure based on an *A* mode. This gives a $++--$ ordering for Mn^{3+} and $-0\ +0$ ordering for Ho^{3+} in the *y* direction. Similar findings is reported for the $R NiO_3$ family where such an ordering scheme is observed in two directions.[27] This situation appears to comply with what could be imagined to happen if k_y for the incommensurate structure is let free to approach and reach $\frac{1}{2}$.

In the G4.1 data from 1.4 K there is a broad peak [full width at half maximum (FWHM) $\approx 3°$] situated between the first two magnetic reflections ($001^{\pm}$ and 110^{-}). Profile fitting of these three peaks shows that FWHM of the broad peak increases with increasing temperature. This is of no importance for the refinements above 10 K. The better resolution of the G4.1 data compared with the D2B data at low scattering angles allows us to see in more detail what is seen as a commensurate additional phase in the D2B data. This additional magnetic intensity is of short-range nature or corresponds to a more or less well-defined magnetic structure with short correlation length. The absence of a satisfactory fit using just peak positions generated for a propagation vector of the form $\mathbf{k}_{com} = (0, \frac{1}{2}, 0)$ may be related to the presence of different propagation vectors in the sample. With the present

data we have not attempted to go more deeply into the search for a model which explains the whole magnetic profile and which may be dominated by both a continuous set of propagation vectors between $k_y = 0.4$ and $k_y = \frac{1}{2}$ and anisotropic peak broadening owing to differences in correlation lengths along different crystallographic directions.

It is appropriate to emphasize that the present value for the holmium moment (some 7.7 μ_B at 1.4–2.8 K, Table I and Fig. 8) is considerable smaller than the free-ion value of 10 μ_B. This deficiency is clearly rooted in the unaccounted amount of moment hidden in the diffuse scattering.

G. Comparison with other rare-earth manganites

According to Quezel *et al.*[19] the magnetic ordering of Mn^{3+} in *o*-$YMnO_3$ is of an incommensurate nature with $\mathbf{k} = 0.458\mathbf{b}^*$. Quezel *et al.* reported that the modulation is of the helical type, but our simulations of the magnetic structure in comparison with the published diffraction diagram[19] contradict this. In order to obtain a helical arrangement a *C*-type mode (see Table III) perpendicular to both the *A* mode and the propagation vector is necessary, and this demands intensity contribution in the form of extra reflections which are not observed. From the actually observed magnetic contributions a longitudinal sinusoidal wave seems probable. Hence the magnetic arrangement of the Mn^{3+} moments in *o*-$HoMnO_3$ and *o*-$YMnO_3$ are similar. This is as expected, owing to the close correspondence in size of Ho^{3+} and Y^{3+}, on the assumption that the Ho^{3+} moments do not have an appreciable influence on the exchange interaction between the Mn^{3+} moments above T_{Ho}.

The magnetic structure of *o*-$HoMnO_3$ is also closely related to that of $TbMnO_3$, which orders as a sinusoidal longitudinal wave with $\mathbf{k} = 0.295\mathbf{b}^*$ below $T_N = 40$ K (A_y above 20 K and both G_x and A_y below 20 K). Tb is short-range ordered below $T_{Tb} = 7$ K with a different wave vector, $\mathbf{k} = 0.415\mathbf{b}^*$. Hence there is less interaction between the Mn^{3+} and R^{3+} moments in $TbMnO_3$ than in *o*-$HoMnO_3$. However, an account for this in terms of exchange integrals is beyond the scope of this paper. Furthermore, it should be noted that there is a different temperature dependence of k_y in $TbMnO_3$ (increasing with the temperature close to T_N) and *o*-$HoMnO_3$. The origin of this distinction is not known.

The magnetic arrangement of the Mn^{3+} moments of $RMnO_3$ with R = La, Pr, Nd, Tb, Ho, and Y are shown in Fig. 10 and the variation in k_y for the same manganites is depicted in Fig. 7. These illustrations brings out a clear correlation between the propagation vector and the size of R^{3+}. In the region of the intermediate sized R^{3+}'s it would be interesting to establish the extension of the commensurate and incommensurate domains. It would indeed also be of considerable interest to follow this trend to the smaller sized R^{3+}'s to see whether k_y continues to increase or get locked in at a commensurate value of, say, $\frac{1}{2}$. Preliminary results for *o*-$ErMnO_3$ indicate that k_y increases to 0.461 (at 7.7 K).

IV. CONCLUSIONS

Finally we should stress that the incommensurate nature of the magnetic structures observed in $RMnO_3$ comes from an increase of the frustration effects due to exchange competitions: the diminution of the Mn-O-Mn superexchange angle owing to the smaller size of the heavy rare earths, which weakens the most significant exchange interaction in the perovskite structure, and consequently the super-superexchange interactions become more important than for the lighter rare earths.

An important point is to explain why the magnetic structures are of the sinusoidal type (fluctuating average magnetic moments) instead of the helical type (constant average magnetic moments). Mn^{3+} has four unpaired electrons, so it is expected that at very low temperature all ions have magnetic moments of $4\mu_B$ and the helical type is to be preferred. The failure to explain the observed diffraction patterns by a helical-type magnetic structure indicates clearly that we have to interpret the sinusoidal structures as the presence of an average structure where only one (or two in the case of Ho) component(s) of the magnetic moments is(are) long-range ordered. The other components are disordered. This may also explain why we have a complicated diffraction pattern at low temperature where the correlation between the disordered components start to increase. Hence diffuse features appear together with well-defined magnetic Bragg reflections. In future experiments we will study the behavior of the magnetic structure below 1.4 K in order to find out if the diffuse commensurate component appearing when Ho starts to order is the real ground state of *o*-$HoMnO_3$.

ACKNOWLEDGMENT

H.W.B. is grateful to The Research Council of Norway for financial support.

*Author to whom correspondence should be addressed.

[1] R. Mahesh, R. Mahendiran, A. K. Raychaudhuri, and C. N. R. Rao, J. Solid State Chem. **120**, 204 (1995).
[2] C. N. R. Rao and A. K. Cheetham, Science **272**, 369 (1996).
[3] H. L. Yakel, W. D. Koehler, E. F. Bertaut, and F. Forrat, Acta Crystallogr. **16**, 957 (1963).
[4] G. Szabo, Ph.D. thesis, University of Lyon, France, 1969.
[5] S. Quezel-Ambrunaz, Bull. Soc. Fr. Mineral. Cristallogr. **91**, 339 (1968).
[6] V. A. Cherepanov, L. Yu Barkhatova, A. N. Petrov, and V. I. Voronin, J. Solid State Chem. **53**, 118 (1995).
[7] W. C. Koehler and E. O. Wollan, J. Phys. Chem. Solids **2**, 100 (1957).
[8] J. Rodríguez-Carvajal, M. Hennion, F. Moussa, A. H. Moudden, L. Pinsard, and A. Revcolevschi, Phys. Rev. B **57**, R3189 (1998).
[9] N. Sakai, H. Fjellvåg, and B. Lebech, Acta Chem. Scand. **51**, 904 (1997).
[10] J. A. Alonso, M. J. Martínez-Lope, M. T. Casais, and M. T. Fernández-Díaz, Inorg. Chem. **39**, 917 (2000).
[11] V. E. Wood, A. E. Austin, E. W. Collings, and K. C. Brog, J. Phys. Chem. Solids **34**, 859 (1973).
[12] H. W. Brinks, H. Fjellvåg, and A. Kjekshus, J. Solid State Chem.

129, 334 (1997).
[13] E. F. Bertaut in *Magnetism*, edited by G. T. Rado and H. Suhl (Academic, New York, 1963), Vol. III, p. 149.
[14] R. Pauthenet and C. Veyret, J. Phys. (Paris) **31**, 65 (1970).
[15] O. Y. Troyanchuk, N. V. Kasper, H. Szymczak, and A. Nabialek, Low Temp. Phys. **23**, 300 (1997).
[16] S. Quezel, F. Tcheou, J. Rossat-Mignod, G. Quezel, and E. Roudaut, Physica B & C **86-88B**, 916 (1977).
[17] Z. Jirák, J. Hejtmánek, E. Pollert, M. Maryško, M. Dlouhá, and S. Vratislav, J. Appl. Phys. **81**, 5790 (1997).
[18] G. Matsumoto, J. Phys. Soc. Jpn. **29**, 606 (1970).
[19] S. Quezel, J. Rossat-Mignod, and E. F. Bertaut, Solid State Commun. **14**, 941 (1974).
[20] J. Rodríguez-Carvajal, program FULLPROF98, Version 0.2 ILL, Grenoble, France, 1998.
[21] J. Töpfer and J. B. Goodenough, J. Solid State Chem. **130**, 117 (1997).
[22] J. Rossat-Mignod, in *Methods of Experimental Physics: Neutron Scattering*, edited by K. Sköld and D. L. Price (Academic, New York, 1987), Vol. 23C.
[23] Y. A. Izyumov, V. E. Naish, and R. P. Ozerov, *Neutron Diffraction of Magnetic Materials* (Consultants Bureau, New York, 1991).
[24] M. J. Freiser, Phys. Rev. **123**, 2003 (1961).
[25] I. Solovyev, N. Hamada, and K. Terakura, Phys. Rev. Lett. **76**, 4825 (1996).
[26] J. B. Goodenough, *Magnetism and the Chemical Bond* (Interscience, New York, 1963).
[27] J. Rodríguez-Carvajal, S. Rosenkranz, M. Medarde, P. Lacorre, M. T. Fernandez-Díaz, F. Fauth, and V. Trounov, Phys. Rev. B **57**, 456 (1998).